Catalysis Letters
https://doi.org/10.1007/s10562-020-03503-6

Morphology Effects of Nanoscale Er_2O_3 and Sr-Er_2O_3 Catalysts for Oxidative Coupling of Methane

Yuqiao Fan[1] · Mingxing Sun[2] · Changxi Miao[3] · Yinghong Yue[1] · Weiming Hua[1] · Zi Gao[1]

Received: 16 October 2020 / Accepted: 16 December 2020

Abstract

Er_2O_3 nanorods were prepared by a hydrothermal method, and Sr-modified Er_2O_3 nanorods (Sr-Er_2O_3) were synthesized using an impregnation method. Their catalytic performance for oxidative coupling of methane was investigated. The catalysts were characterized by several techniques such as XRD, N_2 adsorption, TEM, XPS, O_2-TPD and CO_2-TPD. Compared with Er_2O_3 and Sr-Er_2O_3 nanoparticles, Er_2O_3 and Sr-Er_2O_3 nanorods exhibit higher CH_4 conversion and C_2–C_3 selectivity. This is caused by higher $(O^- + O_2^-)/O^{2-}$ ratio, a higher number of chemisorbed oxygen species and moderate basic sites achieved on the nanorods catalysts. The Sr-Er_2O_3 nanorods afford a 23.2% conversion of CH_4 with 50.3% selectivity to C_2–C_3 at 650 °C.

Graphic Abstract

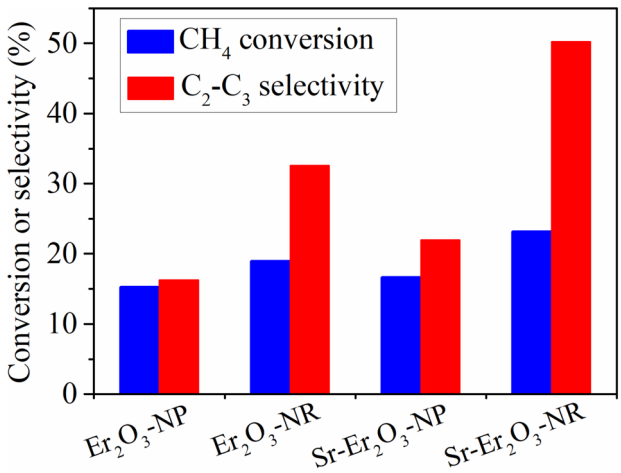

Keywords Er_2O_3-based catalysts · Oxidative coupling of methane · Morphology effect · Crystal plane

1 Introduction

Methane is the main component of natural gas, coal-bed gas and shale gas, which can be converted into high value-added products through non-direct conversion and direct conversion. On the one hand, methane can be first converted into syngas, and further transformed into important basic chemical materials and liquid fuels by Fischer–Tropsch reaction [1, 2]. On the other hand, in the direct conversion technology of methane, most of the research is focused on

Supplementary Information The online version contains supplementary material available at https://doi.org/10.1007/s10562-020-03503-6.

✉ Changxi Miao
miaocx.sshy@sinopec.com

✉ Weiming Hua
wmhua@fudan.edu.cn

Extended author information available on the last page of the article

Published online: 02 January 2021

the direct partial oxidation of methane to methanol [3] or formaldehyde [4], oxidative coupling of methane (OCM) reaction to C_2 hydrocarbons (ethylene and ethane) [5–10], and methane anaerobic aromatization [11, 12]. Owing to the fast consumption of petroleum, the OCM reaction is of great significance and attractive.

OCM was first developed in 1982 by Keller and Bhasin [5]. Since then, hundreds of catalysts have been attempted for OCM. Among them, Li/MgO and Mn-Na_2WO_4/SiO_2 are reported to be the most promising catalysts, and have been extensively studied over the past 30 years [13–28]. However, both types of catalysts generally require high temperature (above 800 °C) to effectively catalyze the OCM reaction. In addition, Li/MgO catalysts still suffer from severe deactivation, due to the vaporization of Li^+ ions at high temperature [19]. Researchers have made an effort to develop the low-temperature OCM catalysts. Wang et al. reported that the Ti-doped Mn-Na_2WO_4/SiO_2 catalyst by using Ti-MWW zeolite as Ti dopant enabled OCM with 26% methane conversion and 76% C_2–C_3 selectivity at 720 °C [29]. Rare earth oxides, such as La_2O_3, Sm_2O_3 and their promoted forms with special morphology, can effectively catalyze the OCM reaction at relatively low temperatures (500–650 °C), although methane conversion and C_2 selectivity and yield are not so satisfactory [30–34].

Er_2O_3 is one kind of rare earth oxide, and there is no report dealing with the use of Er_2O_3 related catalysts for the OCM reaction so far. In this work, Er_2O_3 nanorods, nanoparticles and their respective Sr-modified counterparts were synthesized to catalyze the OCM reaction. The main purpose of this work is to study the morphology effects of Er_2O_3 related catalysts for the OCM reaction. The enhanced reaction performance of Er_2O_3 and Sr-Er_2O_3 nanorods than their nanoparticles counterparts were elucidated based on the physicochemical properties.

2 Experimental

2.1 Catalyst Preparation

The Er_2O_3 nanorods (designated as Er_2O_3-NR) were prepared by a modified hydrothermal method according to the procedures described by Yoon et al. [35]. In a brief, 4.43 g of $Er(NO_3)_3 \bullet 5H_2O$ was dissolved in 100 ml of deionized water, and 5.0 ml of ammonia water was added dropwise to the above 0.1 M Er(III) nitrate solution under stirring. After stirring for additional 0.5 h, the suspension was transferred into a Teflon-lined stainless steel autoclave, sealed and placed in an oven of 200 °C for 12 h. The resulting solid was washed with deionized water, and dried at 110 °C for 12 h. Finally, the dried $Er(OH)_3$ nanorods were calcined in air at 750 °C for 4 h to obtain the Er_2O_3 nanorods. The Er_2O_3 nanoparticles (labelled as Er_2O_3-NP) were synthesized by a conventional precipitation method. 3.0 ml of ammonia water was added dropwise to 100 ml of 0.1 M Er(III) nitrate solution under stirring. After stirring for additional 0.5 h, the resulting precipitate was washed with deionized water, and dried at 110 °C for 12 h. Finally, the dried $Er(OH)_3$ nanoparticles were calcined in air at 750 °C for 4 h to obtain the Er_2O_3 nanoparticles.

The Sr-modified Er_2O_3 nanorods and nanoparticles (denoted as Sr-Er_2O_3-NR and Sr-Er_2O_3-NP, respectively) were prepared by impregnating an aqueous solution of $Sr(NO_3)_2$ on the dried $Er(OH)_3$ nanorods or nanoparticles via an incipient wetness method. The impregnated samples were dried at 110 °C for 12 h and calcined at 750 °C in air for 4 h to obtain the Sr-Er_2O_3-NR and Sr-Er_2O_3-NP catalysts. The molar ratio of Sr to Er in both catalysts was 0.02.

2.2 Catalyst Characterization

X-ray diffraction (XRD) patterns were recorded on a Bruker D2 PHASER X-ray diffractometer using nickel-filtered Cu Kα radiation at 40 kV and 30 mA. The BET surface areas of the samples were analyzed by N_2 adsorption at − 196 °C using a Micromeritics Tristar 3000 instrument. Transmission electron microscopy (TEM) data were obtained on an FEI Tecnai G^2 F20 S-TWIN electron microscope equipped with an EDX instrument. X-ray photoelectron spectroscopy (XPS) measurements were carried out on a Perkin–Elmer PHI 5000C spectrometer with Mg Kα radiation as the excitation source. The O 1 s XPS spectra were fitted using the software XPSPEAK 41, assumed at 20% Lorentzian and 80% Gaussian peak shape. All binding energy values were referenced to the C1s peak located at 284.6 eV. Temperature-programmed desorption of CO_2 (CO_2-TPD) and temperature-programmed desorption of O_2 (O_2-TPD) were performed on a Micromeritics AutoChem II analyzer. 0.2 g of sample (40–60 mesh) was pretreated at 750 °C for 1 h in a He flow. For the CO_2-TPD experiment, the temperature was cooled to 80 °C. Then the flow was switched to 5 vol.% CO_2/He (30 ml/min) and kept at this temperature for 1.5 h, followed by purging with He (30 ml/min) for 2 h. Finally, the temperature was increased from 80 to 900 °C at a heating rate of 10 °C/min. For the O_2-TPD experiment, the temperature was cooled to 50 °C. Then the flow was switched to O_2 (30 ml/min) and kept at this temperature for 1 h, followed by purging with He (30 ml/min) for 2 h. Finally, the temperature was raised from 50 to 700 °C at a ramping rate of 10 °C/min.

2.3 Catalytic Testing

The OCM reaction was carried out in a fixed-bed quartz tube reactor with an internal diameter of 6 mm under ambient pressure. 0.2 g of catalyst (40–60 mesh) was loaded in the

quartz tube, and the downstream of the catalyst was fixed with quartz wool. Prior to the reaction, the catalyst was pretreated at 750 °C for 1 h in a Ar flow. A gas mixture of CH_4 and O_2 (4:1 molar ratio) flowed through the catalyst at a flow rate of 60 ml/min, corresponding to a gas hourly space velocity (GHSV) of 18,000 ml/(g•h). The reaction temperature (that is, catalyst bed temperature) was monitored by a thermocouple placed in the middle of the catalyst bed. The hydrocarbon products were analyzed on-line with a gas chromatograph (GC) equipped with a FID and a 50-m Pora-PLOT Q capillary column (for the separation of CH_4, C_2H_4, C_2H_6, C_3H_6 and C_3H_8), and N_2 was used as the carrier gas. CH_4, H_2, O_2, CO and CO_2 were analyzed on-line by another GC equipped with a TCD and a 2-m Shincarbon ST packed column, and Ar was used as the carrier gas. Before analyzing by TCD, the products were passed through a cold trap at − 3 °C to remove most of water produced in the reaction. The CH_4 conversion and C_2–C_3 selectivity were calculated using the standard normalization method based on carbon atom balance.

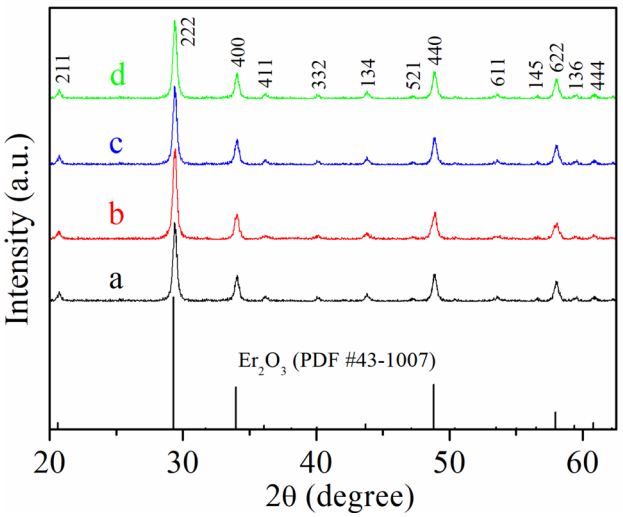

Fig. 1 XRD patterns of (a) Er_2O_3-NP, (b) Er_2O_3-NR, (c) Sr-Er_2O_3-NP, and (d) Sr-Er_2O_3-NR

3 Results and Discussion

3.1 Catalyst Characterization

Figure 1 shows the XRD patterns of Er_2O_3 nanorods, nanoparticles and their respective Sr-modified counterparts. These samples display the characteristic diffractions that match the cubic crystal structure of Er_2O_3 (PDF #43–1007). The diffraction peaks at 2θ = 20.6°, 29.3°, 34.0°, 36.1°, 40.1°, 43.7°, 47.2°, 48.8°, 53.5°, 56.5°, 57.9°, 59.4° and 60.8° can be assigned to the (211), (222), (400), (411), (332), (134), (521), (440), (611), (145), (622), (136) and (444) planes of cubic phase Er_2O_3, respectively. The dominant peak located at 29.3° corresponds to the (222) plane of the crystal phase. It is worth noting that there are no other crystal phases such as SrO and $SrCO_3$ (produced by the combination of SrO with CO_2 in air) which can be detected in all catalysts. One reason is due to the lower content of Sr in the catalysts. Another reason could be that Sr is highly dispersed in the catalysts. The cubic lattice parameters of Er_2O_3-NP and Er_2O_3-NR are 1.0538 nm and 1.0534 nm, respectively, whereas those of Sr-Er_2O_3-NP and Sr-Er_2O_3-NR are somewhat increased to 1.0546 nm and 1.0541 nm, respectively (Table 1). This result is indicative of doping of Sr^{2+} ions into the crystal lattice of cubic Er_2O_3, taking into account the larger ionic radius of Sr^{2+} (0.118 nm) than Er^{3+} (0.089 nm). Similar phenomena were reported for the incorporation of Sr to La_2O_3 and Sm_2O_3 [32, 34, 36].

The TEM images of Er_2O_3-NR, Sr-Er_2O_3-NR, Er_2O_3-NP and Sr-Er_2O_3-NP are shown in Fig. 2. Both Er_2O_3-NR and Sr-Er_2O_3-NR display the nanorod morphology, whereas the morphology of nanoparticles with irregular shape can be observed for both Er_2O_3-NP and Sr-Er_2O_3-NP. The average length and width for Er_2O_3-NR nanorods are 3.34 μm

Table 1 Textural properties and XPS data of the Er_2O_3-based catalysts

Catalyst	S_{BET} (m^2/g)	Average size (μm)	Lattice parameter (nm)	O 1 s BE[c], FWHM[d] (eV)				$(O^- + O_2^-)/O_2^-$
				O^{2-}	O^-	CO_3^{2-}	O_2^-	
Er_2O_3-NP	5.6	0.022 ± 0.003	1.0538	529.2/1.8	530.6/1.6	531.7/1.4	532.7/1.4	0.9
Er_2O_3-NR	8.2	3.34 ± 0.75[a] 0.346 ± 0.065[b]	1.0534	529.4/1.6	530.5/1.7	532.0/1.5	533.0/1.4	1.9
Sr-Er_2O_3-NP	4.5	0.022 ± 0.004	1.0546	529.3/1.6	530.4/1.7	531.7/1.4	532.7/1.5	2.0
Sr-Er_2O_3-NR	8.0	3.29 ± 0.77[a] 0.380 ± 0.063[b]	1.0541	529.3/1.5	530.3/1.9	531.7/1.5	532.7/1.5	2.5

[a]Average length of nanorods. [b]Average width of nanorods

[c]Binding energy. [d]full width at half maximum

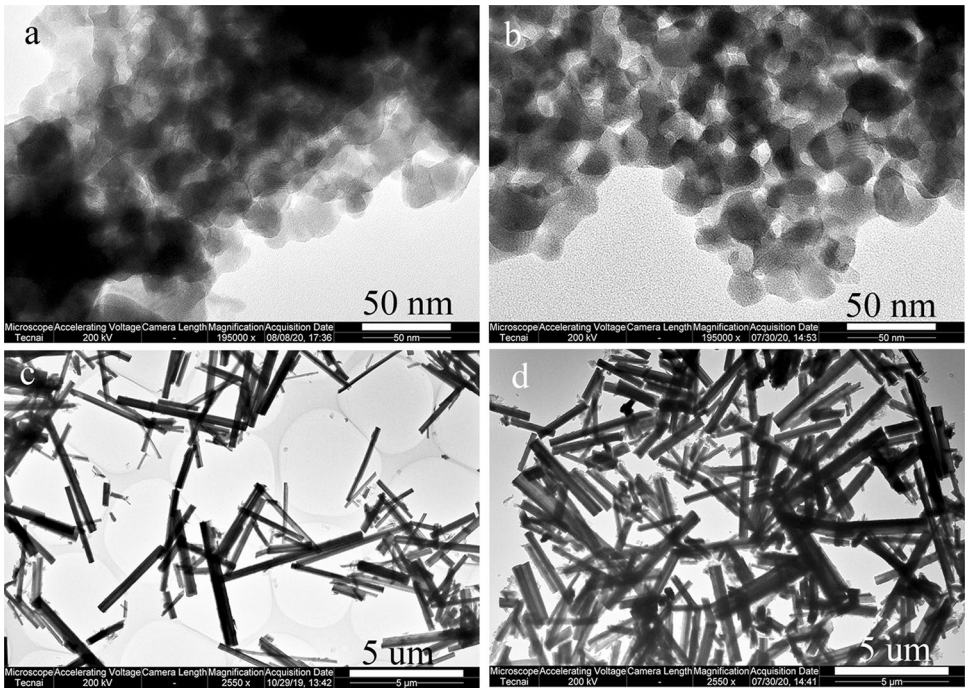

Fig. 2 TEM graphs of **a** Er_2O_3-NP, **b** Sr-Er_2O_3-NP, **c** Er_2O_3-NR, and **d** Sr-Er_2O_3-NR

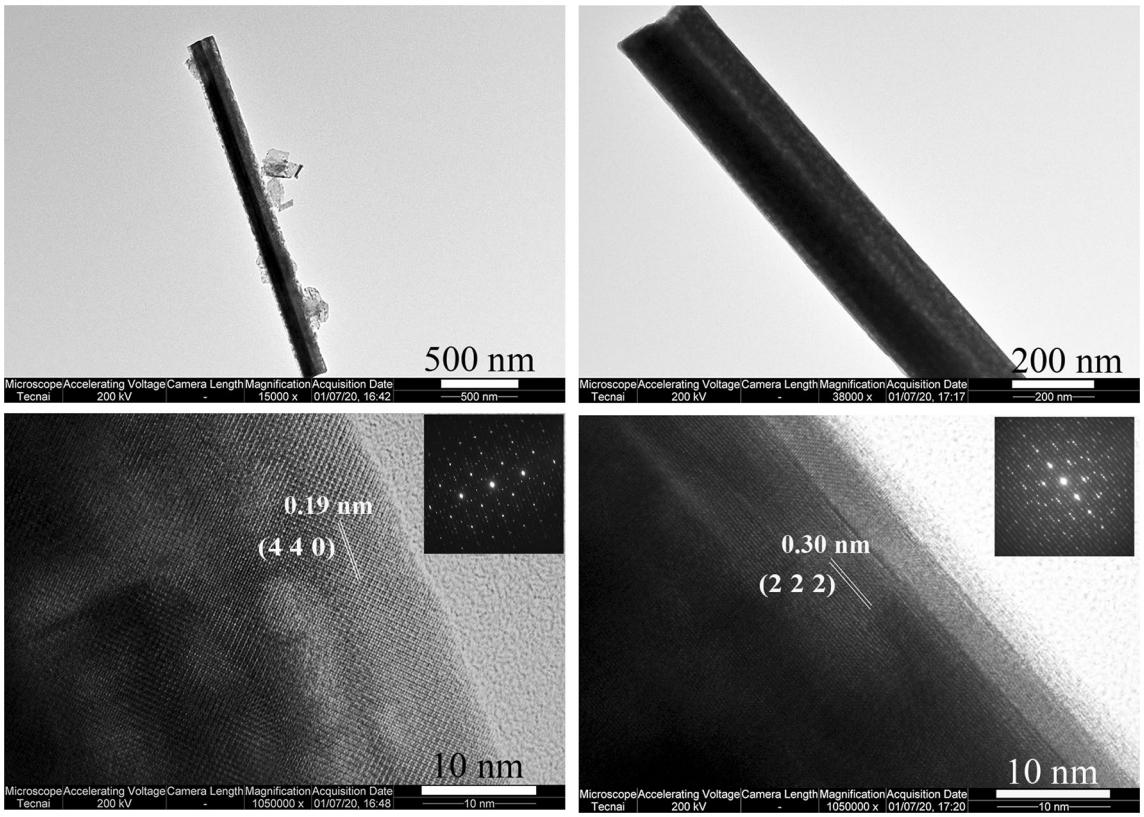

Fig. 3 TEM (top) and HR-TEM (bottom) graphs of Er_2O_3-NR. Insets are the fast Fourier transfer (FFT) patterns of the HR-TEM images

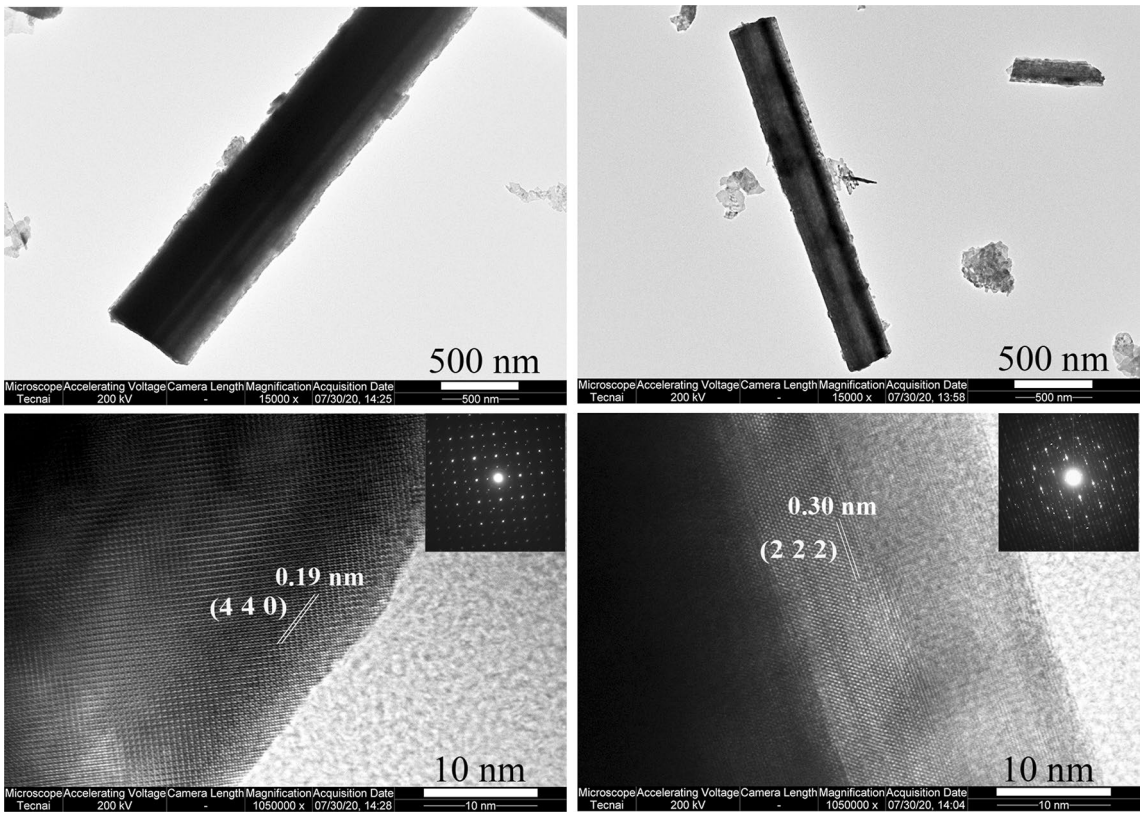

Fig. 4 TEM (top) and HR-TEM (bottom) graphs of Sr-Er_2O_3-NR. Insets are the fast Fourier transfer (FFT) patterns of the HR-TEM images

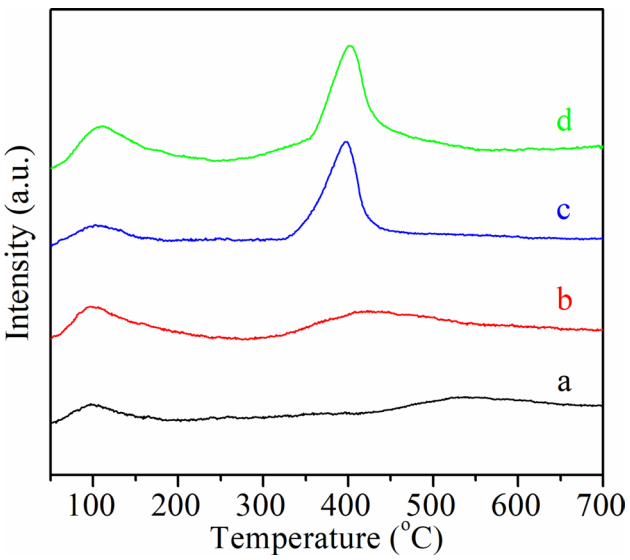

Fig. 5 O_2-TPD profiles of (a) Er_2O_3-NP, (b) Er_2O_3-NR, (c) Sr-Er_2O_3-NP, and (d) Sr-Er_2O_3-NR

and 346 nm, respectively. Er_2O_3-NP nanoparticles have a mean size of 22 nm. It is clear that modification of Er_2O_3 nanorods and nanoparticles with a small amount of Sr has a little impact on their sizes (Fig. 2 and Table 1). As illustrated in Figs. 3 and 4, the HRTEM images combined with a fast Fourier transform (FFT) analysis reveal that Er_2O_3-NR and Sr-Er_2O_3-NR nanorods predominantly expose (440) and (222) planes. A homogeneous distribution of the Sr element in the Sr-modified Sr-Er_2O_3-NR and Sr-Er_2O_3-NP samples is demonstrated by HAADF STEM mapping (Fig. S1).

The BET specific surface areas of the catalysts are given in Table 1. All catalysts possess a low surface area between 4.5 and 8.2 m^2/g, which is typical for the majority of the OCM catalysts. Er_2O_3-NR has a higher surface area than Er_2O_3-NP (8.2 *vs* 5.6 m^2/g). Both Er_2O_3-NR and Sr-Er_2O_3-NR have equivalent surface areas. Modification of Er_2O_3-NP with Sr leads to a slight decrease in surface area.

XPS was employed to elucidate the surface oxygen species on the catalysts. Fig. S2 depicts the XPS spectra of O 1 s on Er_2O_3-NR, Sr-Er_2O_3-NR, Er_2O_3-NP and Sr-Er_2O_3-NP. The XPS spectra were deconvoluted into four peaks at ca. 529.3, 530.5, 531.7 and 532.7 eV which can be assigned to four different oxygen species, i.e. lattice oxygen O^{2-}, peroxide ions O^-, carbonate CO_3^{2-} and superoxide ions O_2^-, respectively [31, 37, 38]. It is generally considered that the surface electrophilic oxygen species O^- and O_2^- are beneficial to the formation of C_2 hydrocarbons of OCM, whereas the lattice oxygen species O^{2-} is responsible for the complete oxidation of CH_4 to CO and CO_2 [31, 33, 39, 40].

Table 2 O_2-TPD and CO_2-TPD data of the Er_2O_3-based catalysts

Catalyst	Peak temperature (°C)		Amount of desorbed O_2 (μmol/g)		Amount of basic sites (μmol/g)		
	I	II	I	II	Weak	Moderate	Strong
Er_2O_3-NP	98	540	7.5	11.8	3.5	4.2	–
Er_2O_3-NR	98	425	27.2	32.1	9.4	8.2	–
Sr-Er_2O_3-NP	102	397	11.2	64.1	3.8	4.2	11.7
Sr-Er_2O_3-NR	109	402	32.4	80.7	8.9	11.4	12.0

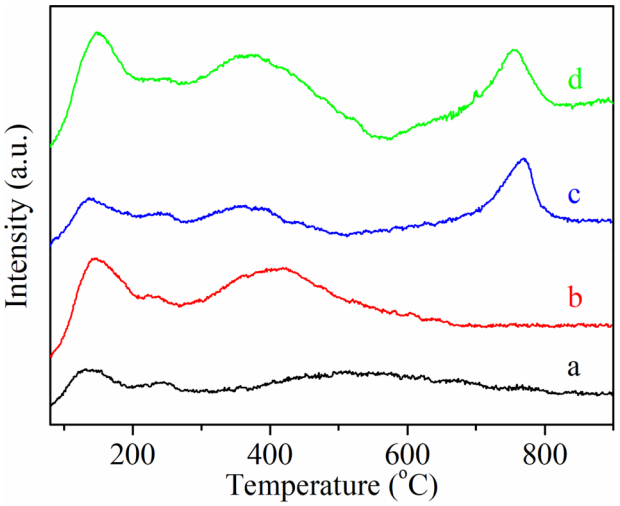

Fig. 6 CO_2-TPD profiles of (a) Er_2O_3-NP, (b) Er_2O_3-NR, (c) Sr-Er_2O_3-NP, and (d) Sr-Er_2O_3-NR

Hence, an increase in the ratio of $(O^- + O_2^-)/O^{2-}$ over the catalysts would favor the C_2 selectivity of OCM [32, 34, 40]. The XPS data presented in Table 1 indicate that Er_2O_3-NR has a higher ratio of $(O^- + O_2^-)/O^{2-}$ than Er_2O_3-NP (1.9 *vs* 0.9). Furthermore, Sr-Er_2O_3-NR has also a higher $(O^- + O_2^-)/O^{2-}$ ratio than Sr-Er_2O_3-NP (2.5 *vs* 2.0). This could be related to the fact that the predominantly exposed planes over Er_2O_3-NR and Sr-Er_2O_3-NR nanorods are (440) and (222) (Figs. 3, 4). Computer simulations have revealed that the energy required to generate oxygen vacancies over CeO_2 is lower on the plane of (110) than (111) [41]. That is to say, oxygen vacancies are more easily to create on the former plane. The interaction of O_2 with oxygen vacancies generates surface oxygen species such as O^- and O_2^- which play a significant role in OCM reaction. Wan and co-authors reported that the exposed (110), (1 $\bar{2}$ 0), and (2 $\bar{1}$ 0) facets on the $La_2O_2CO_3$ catalysts were beneficial to the formation of the chemisorbed oxygen species [38]. On the other hand, modification of Er_2O_3-NR and Er_2O_3-NP with Sr leads to an improvement in the $(O^- + O_2^-)/O^{2-}$ ratio. Reportedly, doping Sr into La_2O_3 brought about the similar result [32, 34].

In order to discern the oxygen activation over Er_2O_3 nanorods, nanoparticles and their respective Sr-doped counterparts which plays a key role in OCM reaction, the O_2-TPD measurements were performed. As illustrated in Fig. 5, there are two desorption peaks on the TPD profiles. The low temperature peaks at about 100 °C correspond to the desorption of molecular oxygen, whereas the high temperature ones at 400–540 °C are assigned to the desorption of chemisorbed oxygen species (such as O^- and O_2^- [34, 42]) which are helpful for the activation of CH_4 and C_2 selectivity in OCM reaction [31, 38, 42, 43]. Thus, higher CH_4 conversion of OCM would be expected over the catalysts possessing more sites for chemisorbed oxygen adsorption. The O_2-TPD data (Table 2) shows that the amount of chemisorbed oxygen species is higher over Er_2O_3-NR than Er_2O_3-NP (32.1 vs 11.8 μmol/g), and over Sr-Er_2O_3-NR than Sr-Er_2O_3-NP (80.7 vs 64.1 μmol/g). It can be also seen that the amount of chemisorbed oxygen species over Er_2O_3-NR and Er_2O_3-NP is enhanced upon Sr modification. The similar phenomena were found in the case of incorporation of Sr to La_2O_3 [32, 34].

The TPD of CO_2 was conducted to investigate the surface basic sites of Er_2O_3 nanorods, nanoparticles and their respective Sr-doped counterparts which are important for an effective OCM catalyst [36, 44]. These basic sites originate from surface O^{2-}, O_2^- and O^- [14, 36, 45]. As presented in Fig. 6, there are three peaks of CO_2 desorption at about 140 °C, 370 °C and 760 °C for Sr-Er_2O_3-NR and Sr-Er_2O_3-NP which correspond to the weak, moderate and strong basic sites present on the catalysts, respectively. Er_2O_3-NR and Er_2O_3-NP possess only weak and medium basic sites. It is believed that the surface basic sites with moderate and strong strength are beneficial to both CH_4 activation and C_2 product formation in OCM reaction [31, 34, 36, 38, 43, 44, 46, 47]. The CO_2-TPD data (Table 2) shows that the number of moderate basic sites is greater on Er_2O_3-NR than Er_2O_3-NP (8.2 *vs* 4.2 μmol/g), and on Sr-Er_2O_3-NR than Sr-Er_2O_3-NP (11.4 *vs* 4.2 μmol/g). Both Sr-Er_2O_3-NR than Sr-Er_2O_3-NP have equivalent strong basic sites. The addition of Sr to Er_2O_3-NR and Er_2O_3-NP results in an enhanced number of strong or moderate basic sites.

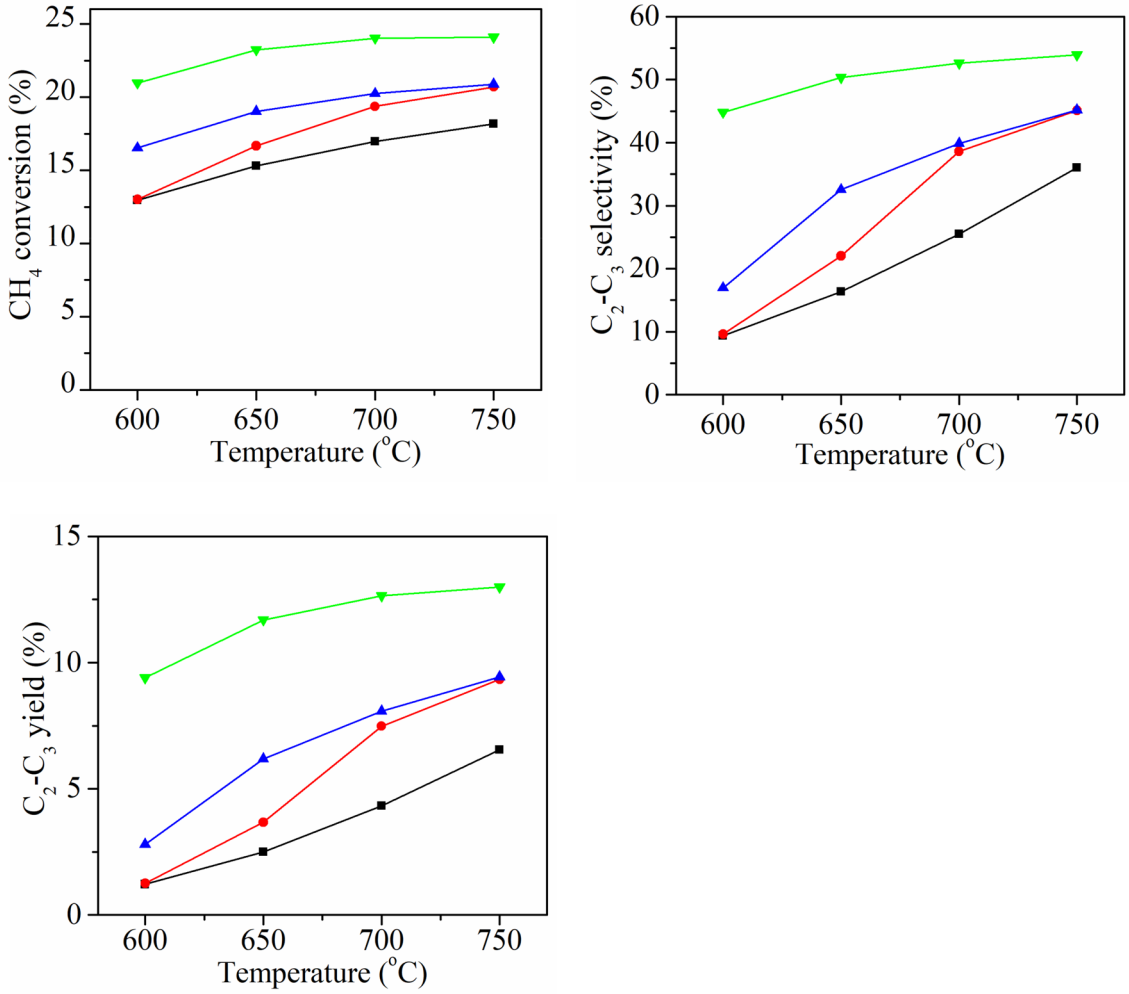

Fig. 7 CH_4 conversion, C_2-C_3 selectivity and C_2-C_3 yield as a function of reaction temperature for the Er_2O_3-based catalysts. (■) Er_2O_3-NP, (▲) Er_2O_3-NR, (●) Sr-Er_2O_3-NP, (▼) Sr-Er_2O_3-NR

Table 3 Reaction data of the Er_2O_3-based catalysts at 650 °C

Catalyst	Conversion of CH_4 (%)	Selectivity (%)						Selectivity of C_2-C_3 (%)	Yield of C_2-C_3 (%)
		C_2H_4	C_2H_6	C_3H_6	C_3H_8	CO_2	CO		
Er_2O_3-NP	15.3	4.9	10.4	0.6	0.4	47.8	35.9	16.3	2.5
Er_2O_3-NR	19.0	14.5	16.6	1.0	0.5	43.9	23.5	32.6	6.2
Sr-Er_2O_3-NP	16.7	7.0	13.8	0.7	0.5	53.5	24.5	22.0	3.7
Sr-Er_2O_3-NR	23.2	25.4	21.9	2.2	0.8	39.9	9.8	50.3	11.7

3.2 Catalytic Performance

Figure 7 shows the results of OCM reaction over Er_2O_3 nanorods, nanoparticles and their respective Sr-doped counterparts at different temperatures. The main hydrocarbon products are C_2H_4 and C_2H_6, and minor amounts of C_3H_6 and C_3H_8 were also detected. The by-products are CO and CO_2. The typical product distribution over the catalysts at a reaction temperature of 650 °C is given in Table 3.

As the reaction temperature is increased from 600 °C to 750 °C, the CH_4 conversion improves gradually. In contrast, the selectivity of C_2–C_3 (C_2H_4, C_2H_6, C_3H_6 and C_3H_8) increases more obviously. Correspondingly, the C_2–C_3 yield also rises with the reaction temperature. Regardless of CH_4 conversion, C_2–C_3 selectivity or yield, Er_2O_3-NR and Sr-Er_2O_3-NR nanorods perform better than Er_2O_3-NP and Sr-Er_2O_3-NP nanoparticles, respectively, which is indicative of shape effects of Er_2O_3 and Sr-Er_2O_3 nanocatalysts

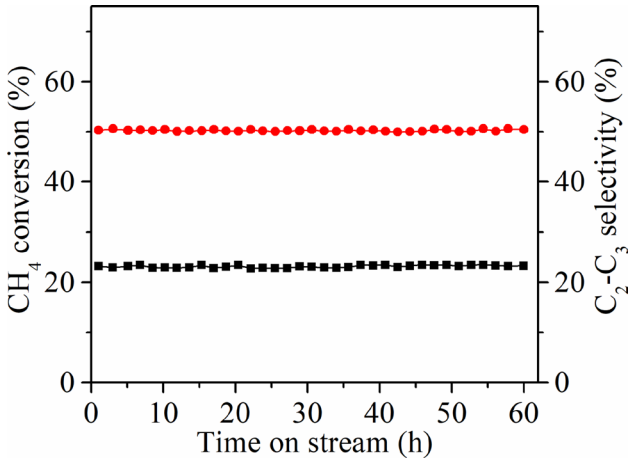

Fig. 8 CH_4 conversion (■) and C_2-C_3 selectivity (●) with time on stream over Sr-Er_2O_3-NR at 650 °C

for OCM reaction. For example, Er_2O_3-NR nanorods give a 20.2% conversion of CH_4 with 39.9% selectivity and 8.1% yield to C_2–C_3 at 700 °C, while Er_2O_3-NP nanoparticles afford a 17.0% conversion of CH_4 with 25.5% selectivity and 4.3% yield to C_2–C_3. The CH_4 conversion, C_2–C_3 selectivity and yield are 24.0%, 52.6% and 12.6%, respectively, for Sr-Er_2O_3-NR nanorods at 700 °C, whereas they are 19.4%, 38.6% and 7.5%, respectively, for Sr-Er_2O_3-NP nanoparticles. Reportedly, La_2O_3 catalysts also displayed morphology effects for OCM reaction [31, 33]. Taking into account the above XPS, O_2-TPD and CO_2-TPD results, the better reaction performance over Er_2O_3-NR and Sr-Er_2O_3-NR nanorods is caused by their higher $(O^- + O_2^-)/O^{2-}$ ratio, more chemisorbed oxygen species and moderate basic sites. These reasons are also responsible for the enhanced reaction performance of Er_2O_3-NR and Er_2O_3-NP catalysts upon Sr modification, as can be seen from Fig. 7.

The stability of the best catalyst Sr-Er_2O_3-NR was evaluated at 650 °C, and the results are shown in Fig. 8. As can be seen, the Sr-Er_2O_3-NR catalyst displays good stability in OCM reaction for 60 h of time on stream, affording ca. 23% conversion of CH_4 with around 50% selectivity to C_2–C_3. As revealed in Figs. S3 and S4a, almost no changes can be observed in TEM images and XRD patterns of the fresh and spent Sr-Er_2O_3-NR catalysts. After the stability test, the surface area of Sr-Er_2O_3-NR is 7.8 m^2/g which is equivalent to that of the fresh catalyst (8.0 m^2/g). These facts demonstrate the maintenance of the catalyst structure after the stability test. Moreover, there are almost no differences in the O 1 s XPS spectra of fresh and spent Sr-Er_2O_3-NR catalysts (Fig. S4b), indicating that the surface species did not alter during the OCM reaction.

A reference catalyst (Sr-La_2O_3 nanofibers) was prepared according to the literature [32]. The Sr content was selected to be 8.6 wt.%, because Sr-La_2O_3 nanofibers with this content of Sr exhibited the highest methane conversion and C_2 selectivity for OCM reaction [32]. We tested the performance of Sr-La_2O_3 nanofibers under our reaction conditions, and compared with the Sr-Er_2O_3-NR catalyst in this work. As illustrated in Fig. 9, Sr-Er_2O_3-NR exhibits higher C_2–C_3 selectivity and a bit greater methane conversion than Sr-La_2O_3 at 600 and 650 °C. However, the former catalyst displays lower C_2-C_3 selectivity and a bit lower methane conversion than Sr-La_2O_3 at 700 and 750 °C.

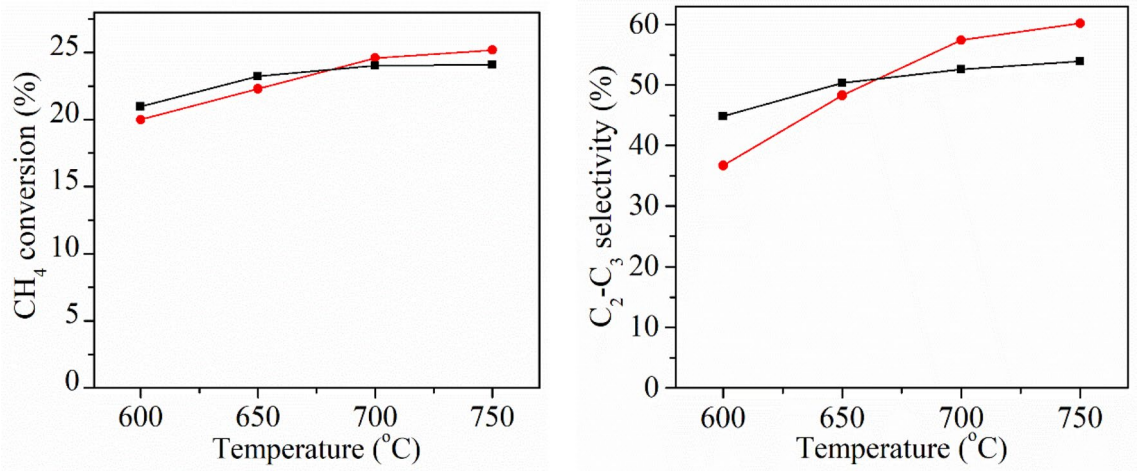

Fig. 9 Comparison of Sr-Er_2O_3-NR (■) and Sr-La_2O_3 (●) catalysts for CH_4 conversion and C_2-C_3 selectivity as a function of reaction temperature

4 Conclusions

In this work, we have demonstrated that Er_2O_3 and Sr-Er_2O_3 nanorods outperform Er_2O_3 and Sr-Er_2O_3 nanoparticles, respectively, for oxidative coupling of methane. The XRD and HAADF STEM mapping results reveal the homogeneous distribution of Sr element in Sr-Er_2O_3 nanorods and nanoparticles. The HRTEM images reveal that Er_2O_3 and Sr-Er_2O_3 nanorods predominantly expose (440) and (222) planes. The $(O^- + O_2^-)/O^{2-}$ ratio, amount of chemisorbed oxygen species and moderate basic sites are greater on Er_2O_3 nanorods than Er_2O_3 nanoparticles, and on Sr-Er_2O_3 nanorods than Sr-Er_2O_3 nanoparticles, as revealed by XPS, O_2-TPD and CO_2-TPD, respectively. These reasons are responsible for the superior reaction performance of Er_2O_3 and Sr-Er_2O_3 nanorods to their nanoparticles counterparts. A 23.2% conversion of CH_4 with 50.3% selectivity to C_2–C_3 can be achieved over Sr-Er_2O_3 nanorods at 650 °C.

Acknowledgements This work was supported financially by the National Key R&D Program of China (2017YFB0602200), the National Natural Science Foundation of China (91645201), the Science and Technology Commission of Shanghai Municipality (19DZ2270100), the Shanghai Research Institute of Petrochemical Technology SINOPEC (19ZC06070005), and the Science and Technology Project of General Administration of Customs of China (2019HK059).

References

1. Velasco JA, Lopez L, Velásquez M, Boutonnet M, Cabrera S, Järås S (2010) J Nat Gas Sci Eng 2:222
2. Maqbool W, Park SJ, Lee ES (2014) Ind Eng Chem Res 53:9454
3. Han B, Yang Y, Xu Y, Etim UJ, Qiao K, Xu B, Yan Z (2016) Chin J Catal 37:1206
4. Horn R, Schlögl R (2015) Catal Lett 145:23
5. Keller GE, Bhasin MM (1982) J Catal 73:9
6. Lunsford JH (1995) Angew Chem Int Ed 34:970
7. Mesters C (2016) Annu Rev Chem Biomol Eng 7:223
8. Aseem A, Jeba GG, Conato MT, Rimer JD, Harold MP (2018) Chem Eng J 331:132
9. Galadima A, Muraza O (2016) J Ind Eng Chem 37:1
10. Gambo Y, Jalil AA, Triwahyono S, Abdulrasheed AA (2018) J Ind Eng Chem 59:218
11. Guo X, Fang G, Li G, Ma H, Fan H, Yu L, Ma C, Wu X, Deng D, Wei M, Tan D, Si R, Zhang S, Li J, Sun L, Tang Z, Pan X, Bao X (2014) Science 344:616
12. Zhang JZ, Long MA, Howe RF (1998) Catal Today 44:293
13. Ito T, Lunsford JH (1985) Nature 314:721
14. Driscoll DJ, Martir W, Wang JX, Lunsford JH (1985) J Am Chem Soc 107:58
15. Peil KP, Goodwin JG, Marcelin G (1991) J Catal 131:143
16. Nagaoka K, Karasuda T, Aika K (1999) J Catal 181:160
17. Amin NAS, Pheng SE (2006) Chem Eng J 116:187
18. Tang L, Yamaguchi D, Wong L, Burke N, Chiang K (2011) Catal Today 178:172
19. Arndt S, Simon U, Kiefer K, Otremba T, Siemensmeyer K, Wollgarten M, Berthold A, Schmidt F, Görke O, Schomäcker R, Dinse KP (2017) ChemCatChem 9:3583
20. Fang X, Li S, Lin J, Gu J, Yan D (1992) J Mol Catal 6:254
21. Ji S, Xiao T, Li S, Chou L, Zhang B, Xu C, Hou R, York APE, Green MLH (2003) J Catal 220:47
22. Wang J, Chou L, Zhang B, Song H, Zhao J, Yang J, Li S (2006) J Mol Catal A 245:272
23. Arndt S, Otremba T, Simon U, Yildiz M, Schubert H, Schomäcker R (2012) Appl Catal A 425–426:53
24. Ghose R, Hwang HT, Varma A (2014) Appl Catal A 472:39
25. Elkins TW, Hagelin-Weaver HE (2015) Appl Catal A 497:96
26. Fleischer V, Steuer R, Parishan S, Schomäcker R (2016) J Catal 341:91
27. Arndt S, Laugel G, Levchenko S, Horn R, Baerns M, Scheffler M, Schlögl R, Schomäcker R (2011) Catal Rev Sci Eng 53:424
28. Werny MJ, Wang Y, Girgsdies F, Schlögl R, Trunschke A (2020) Angew Chem Int Ed 59:14921
29. Wang P, Zhao G, Wang Y, Lu Y (2017) Sci Adv 3:e1603180
30. Fu B, Jiang T, Zhu Y (2018) J Nanosci Nanotechnol 18:3398
31. Huang P, Zhao Y, Zhang J, Zhu Y, Sun Y (2013) Nanoscale 5:10844
32. Song J, Sun Y, Ba R, Huang S, Zhao Y, Zhang J, Sun Y, Zhu Y (2015) Nanoscale 7:2260
33. Jiang T, Song J, Huo M, Yang N, Liu J, Zhang J, Sun Y, Zhu Y (2016) RSC Adv 6:34872
34. Zhao M, Ke S, Wu H, Xia W, Wan H (2019) Ind Eng Chem Res 58:22847
35. Yoon HJ, Lee J, Kim Y, Cho DW, Sohn Y (2017) Ceram Int 43:2069
36. Papa F, Luminita P, Osiceanu P, Birjega R, Akane M, Balint I (2011) J Mol Catal A 346:46
37. Kharas KCC, Lunsford JH (1989) J Am Chem Soc 111:2336
38. Hou YH, Han WC, Xia WS, Wan HL (2015) ACS Catal 5:1663
39. Ding W, Chen Y, Fu X (1994) Catal Lett 23:69
40. Bai Y, Xia W, Weng W, Lian M, Zhao M, Wan H (2018) Chem J Chin Univ Chin 39:247
41. Sayle TXT, Parker SC, Sayle DC (2005) Phys Chem Chem Phys 7:2936
42. Spinicci R, Tofanari A (1990) Catal Today 6:473
43. Xu J, Zhang Y, Xu X, Fang X, Xi R, Liu Y, Zheng R, Wang X (2019) ACS Catal 9:4030
44. Elkins TW, Roberts SJ, Hagelin-Weaver HE (2016) Appl Catal A 528:175
45. Bernal S, Blanco G, El Amarti A, Cifredo G, Fitian L, Galtayries A, Martín J, Pintado JM (2006) Surf Interface Anal 38:229
46. Hou YH, Lin YL, Li Q, Weng WZ, Xia WS, Wan HL (2013) ChemCatChem 5:3725
47. Peng L, Xu J, Fang X, Liu W, Xu X, Liu L, Li Z, Peng H, Zheng R, Wang X (2018). Eur J Inorg Chem. https://doi.org/10.1002/ejic.201701440

Affiliations

Yuqiao Fan[1] · Mingxing Sun[2] · Changxi Miao[3] · Yinghong Yue[1] · Weiming Hua[1] · Zi Gao[1]

Yuqiao Fan
18110220090@fudan.edu.cn

Mingxing Sun
sunmxing@vip.163.com

Yinghong Yue
yhyue@fudan.edu.cn

Zi Gao
zigao@fudan.edu.cn

[1] Shanghai Key Laboratory of Molecular Catalysis and Innovative Materials, Department of Chemistry, Fudan University, Shanghai 200438, PR China

[2] Shanghai Customs Technology Center of Inspection and Test, Shanghai 200120, PR China

[3] Shanghai Research Institute of Petrochemical Technology SINOPEC, Shanghai 201208, PR China